The Astrophysical Journal, 968:42 (12pp), 2024 June 10 https://doi.org/10.3847/1538-4357/ad3e86

Discovery of a Proto–White Dwarf with a Massive Unseen Companion

Gautham Adamane Pallathadka[1], Vedant Chandra[2], Nadia L. Zakamska[1], Hsiang-Chih Hwang[3], Yossef Zenati[1], J. J. Hermes[4], Kareem El-Badry[5], Boris T. Gänsicke[6], Sean Morrison[7], Nicole R. Crumpler[1], and Stefan Arseneau[1]
[1] William H. Miller III Department of Physics & Astronomy, Johns Hopkins University, 3400 N Charles St, Baltimore, MD 21218, USA; gadaman1@jh.edu
[2] Center for Astrophysics, Harvard & Smithsonian, 60 Garden St, Cambridge, MA 02138, USA
[3] School of Natural Sciences, Institute for Advanced Study, Princeton, 1 Einstein Drive, NJ 08540, USA
[4] Department of Astronomy, Boston University, 725 Commonwealth Ave., Boston, MA 02215, USA
[5] Department of Astronomy, California Institute of Technology, 200 E. California Blvd., Pasadena, CA 91125, USA
[6] Department of Physics, University of Warwick, Coventry CV4 7AL, UK
[7] Department of Astronomy, University of Illinois at Urbana-Champaign, Urbana, IL 61801, USA
Received 2023 October 23; revised 2024 February 19; accepted 2024 April 4; published 2024 June 7

Abstract

We report the discovery of SDSS J022932.28+713002.7, a nascent extremely low-mass (ELM) white dwarf (WD) orbiting a massive (>1 $M_\odot$ at 2σ confidence) companion with a period of 36 hr. We use a combination of spectroscopy, including data from the ongoing fifth-generation Sloan Digital Sky Survey (SDSS-V), and photometry to measure the stellar parameters of the primary pre-ELM WD. The lightcurve of the primary WD exhibits ellipsoidal variation, which we combine with radial velocity data and PHOEBE binary simulations to estimate the mass of the invisible companion. We find that the primary WD has mass $M_1 = 0.18^{+0.02}_{-0.02}\ M_\odot$ and the unseen secondary has mass $M_2 = 1.19^{+0.21}_{-0.14}\ M_\odot$. The mass of the companion suggests that it is most likely a near-Chandrasekhar-mass WD or a neutron star. It is likely that the system recently went through a Roche lobe overflow from the visible primary onto the invisible secondary. The dynamical configuration of the binary is consistent with the theoretical evolutionary tracks for such objects, and the primary is currently in its contraction phase. The measured orbital period puts this system on a stable evolutionary path which, within a few gigayears, will lead to a contracted ELM WD orbiting a massive compact companion.

Unified Astronomy Thesaurus concepts: Binary stars (154); White dwarf stars (1799); Neutron stars (1108); Low mass stars (2050)

Supporting material: data behind figure

1. Introduction

White dwarfs (WDs) are remnants left behind by main-sequence stars with masses in the range 0.8–8 $M_\odot$. While the typical masses of WDs range from 0.5 $M_\odot$ up to 1.4 $M_\odot$, extremely low-mass white dwarfs (ELM WDs) with masses in 0.15–0.35 $M_\odot$ have been detected in binaries (Iben & Tutukov 1985; Brown et al. 2010; Istrate et al. 2016; El-Badry et al. 2021). These ELM WDs are usually formed when a massive main-sequence star loses its outer envelope to a companion. The helium core that remains with a hydrogen atmosphere is an ELM WD (Nelson et al. 2004; Li et al. 2019). They have been theorized to form only in binary systems—their mass is too low to be formed from single star evolution within a Hubble time—and this scenario is supported by observations as well (Marsh et al. 1995; Brown et al. 2010).

ELM WDs can be found in binaries with WDs (Brown et al. 2020), pulsars (Nelson et al. 2004; Antoniadis et al. 2013; Istrate et al. 2014a), or main-sequence stars (Maxted et al. 2011). These binaries are interesting because they help us piece together the evolutionary pathways and test our understanding of binary evolution. Compact binaries of double WDs are particularly interesting since they are possible Type Ia supernova progenitors (Nomoto 1984; Maoz et al. 2014; Jha et al. 2019; Soker 2019). They are also dominant sources of low-frequency gravitational waves for future observatories like the Laser Interferometer Space Antenna (Marsh 2011; Korol et al. 2022). WD mergers with neutron stars (NSs) or black holes are candidate progenitors of gamma-ray bursts or other types of explosive transients (Fryer et al. 1999; Margalit & Metzger 2016; Bobrick et al. 2017, 2022; Zenati et al. 2019, 2020; Kaltenborn et al. 2022). In binaries with pulsars, the mass transfer phase can lead to spin-up of the pulsar, giving birth to millisecond pulsars. These systems can be used to independently verify the spin-down age of millisecond pulsars (Nelson et al. 2004).

While ELM WDs have surface gravity values in the range $\log g$ = 5–6.5 (where g is in cgs units), in the early stages of their evolution they can appear as bloated pre-ELM WDs with a smaller $\log g$ (Kupfer et al. 2020a, 2020b; Lagos et al. 2020; Wang et al. 2020; El-Badry et al. 2021). Using spectroscopic and photometric data one can solve for the parameters of the visible object, hereafter called the primary. Without additional information it is not possible to solve for the mass of the invisible—secondary—object because of a degeneracy between the mass of the secondary and the system's inclination. Because of their bloated nature, the surfaces of pre-ELM WDs can be tidally distorted in the presence of a companion. This change in the shape of the stellar surface leads to a periodic variation in the lightcurve. Therefore, the mass–inclination degeneracy can be further constrained with lightcurve data.

In this paper we report the discovery of SDSS J022932.29+713002.6 (hereafter SDSS J0229+7130), a binary consisting

of a bloated pre-ELM WD and an invisible companion with a mass close to and perhaps exceeding the Chandrasekhar mass. We summarize the observations in Section 2. We analyze them and present measurements of the binary parameters in Section 3. We discuss the results in Section 4. Throughout the paper g is the acceleration due to gravity in cgs units (cm s^{-2}), [Fe/H] is the abundance ratio relative to the Sun on a logarithmic scale, Z is the metallicity of the star, i.e., the mass fraction of metals on a linear scale, and $T_{\rm eff}$ is the stellar temperature in Kelvin. Inclination angles are measured relative to the plane of the sky, so that $i = 90°$ is an edge-on system. We refer to the less massive WD as being the primary component, and the secondary is the more massive invisible companion.

2. Observations and Data Reduction

2.1. Spectroscopic Data

We identified SDSS J0229+7130 in the first-year data from the Milky Way Mapper, a multiepoch Galactic spectroscopic program in the fifth-generation Sloan Digital Sky Survey (SDSS-V; Kollmeier et al. 2017, 2019). Milky Way Mapper started in 2020 November using the Apache Point Observatory (APO) 2.5 m telescope (Gunn et al. 2006) and is now also operating at the Las Campanas Observatory 2.5 m telescope (Bowen & Vaughan 1973) using both the Baryon Oscillation Spectroscopic Survey (BOSS) spectrograph (Smee et al. 2013) and the APO Galactic Evolution Experiment spectrographs (Wilson et al. 2019). Our target was observed for a total of nine individual exposures between 2020 December 4 and 2020 December 6 with BOSS. Each exposure lasted 900 s and covered a wavelength range from 3600 to 10000 Å at a resolution of $R \simeq 1800$. The wavelengths of the spectra are corrected to the heliocentric frame, and the absolute wavelength calibration of each exposure is accurate to <10 km s^{-1}. The BOSS data products in this paper were derived by using `IDLspec2D v6_1_0`.

We initially flagged SDSS J0229+7130 due to its significant radial velocity (RV) variation of $\gtrsim$100 km s^{-1} between different nights, albeit with minimal variation across successive exposures on a given night. This suggested that both the RV amplitude and orbital period are large, hallmarks of a high-mass-function binary. Spectroscopically, SDSS J0229+7130 looks like a pure hydrogen atmospheric DA WD, with narrow Balmer lines (Figure 1). In addition, there is a faint sodium absorption doublet Na I D near 6000 Å and calcium absorption line Ca II K near 3933 Å, which are discussed further in Section 3.1.

Although the SDSS-V data suggested a high-mass-function binary, the RV data were too sparse to better constrain the mass function and definitively measure the orbital period. To fill in the orbital phase coverage, we obtained follow-up spectroscopy with the Dual-Imaging Spectrograph on the 3.5 m telescope at APO. We used the B1200/R1200 gratings with a 1.″5 slit, delivering resolution $R \approx 3000$. We obtained 20, 900 s exposures between three different nights on 2021 October 5, 2021 November 1, and 2021 November 5. The APO data were reduced by the standard IRAF pipeline.

The absolute wavelength calibration of the APO spectra showed systematic shifts, which increased with the wavelength. To account for this, we estimate the shift at 6498 Å (close to the Hα line) using the known positions of the sky lines, and measure the RVs incorporating this derived correction. We also increase the RV error by adding this correction in quadrature to the measured RV error, to get the most conservative RV uncertainties. The RVs for APO data are corrected to barycentric frame using the package `barycorrpy`[8] (Corrales 2015; Kanodia & Wright 2018). The low-wavelength end of the APO spectra had issues and is unreliable. We only use data with a wavelength greater than 5900 Å.

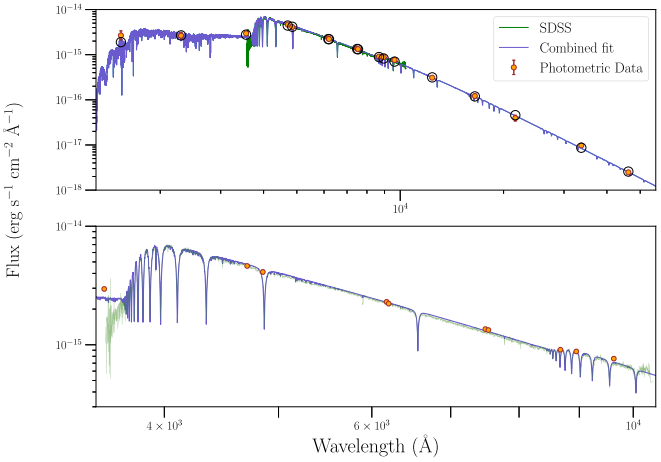

Figure 1. The flux-corrected coadded SDSS spectrum (green line) and archival photometry (orange points) are shown along with the best-fit theoretical spectrum (blue line). The bottom panel shows the spectral region covered by the SDSS spectroscopic data. The spectral data obtained for this work are available as the data behind the figure in the online journal. These data include both the SDSS and APO spectra.

(The data used to create this figure are available.)

2.2. Photometric Data

Our target is at a distance of $d = 1.66 \pm 0.12$ kpc, which is calculated by Bailer-Jones et al. (2021) using the Gaia parallax measurement (Gaia Collaboration et al. 2023). Looking at the Gaia color–magnitude diagram (Figure 2), we see that the object lies well above the WD track, and is only slightly below the main sequence. Thus, based on the spectra and the position of the star on the Gaia color–magnitude diagram, we propose that this object is neither a typical WD nor a main-sequence star. There are no resolved wide companions (at separation >2000 au) near our target in Gaia, and there are no astrometric anomalies reported in Gaia DR3 for this source. So there is no evidence for additional companions to the spatially unresolved system. The object is close to the plane of the Galaxy with $b \approx 10°$, and given the inferred distance we need to carefully take into account the interstellar extinction, as explained in detail in Section 3.

In addition to the spectroscopic data, this object has archival Zwicky Transient Facility (ZTF) observations (Masci et al. 2019; IRSA 2022), and we selected all observations released in DR18. The object was observed with the g filter between 2018 June 29 and 2023 February 20, and between 2018 June 14 and 2023 March 10 with the r filter. To select clean data, we choose all point sources in ZTF within 5″ of the target position obtained from Gaia with ZTF quality flag `catflags` $= 0$ and $|$`sharp`$| < 0.25$. We find that all the available data points correspond to our object and are within 5″ of our target.

[8] https://github.com/shbhuk/barycorrpy

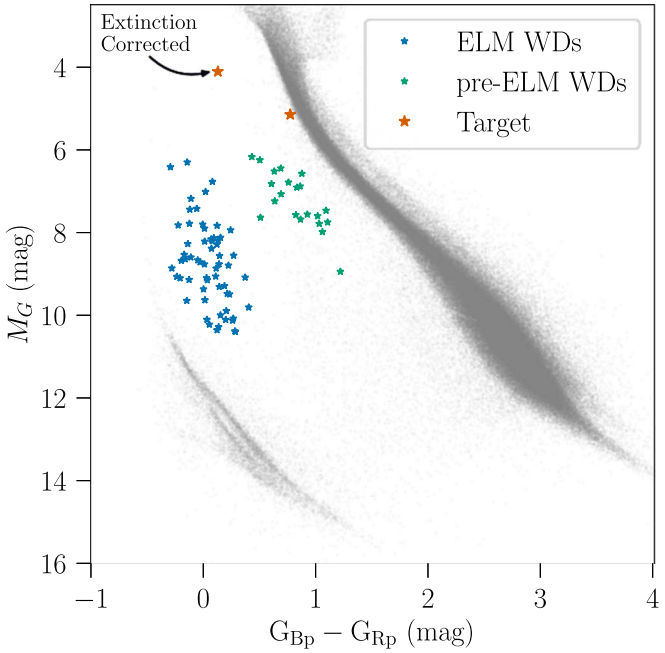

Figure 2. Color–magnitude diagram. Our target is marked in brown. We also show the extinction-corrected position. The blue points are ELM WDs from Brown et al. (2020) and the green points are pre-ELM WDs from El-Badry et al. (2021). The sequence in the lower left, below the ELM candidates, is the normal WD track. Our target is just below the main sequence.

However, quality cuts reduce the number of data points from 912 to 821, and we obtain a clean ZTF lightcurve.

This object also has archival Transiting Exoplanet Survey Satellite (TESS; Ricker et al. 2015) observations in the Full Frame Image (FFI) data in Sectors 18 and 19 (STScI 2019, 2020). The data in Sector 18 have instrumental artifacts and hence we restrict ourselves to data from Sector 19. We obtain the lightcurve from the FFIs using `eleanor`[9] (Brasseur et al. 2019; Feinstein et al. 2019).

We collect archival photometric data for this object using VizieR[10] (Ochsenbein et al. 2000). This object has photometric data from SDSS in the *ugriz* filters (Ahumada et al. 2020), from the Two Micron All Sky Survey (2MASS) in the JHK_s filters (Skrutskie et al. 2006), from the Galaxy Evolution Explorer (GALEX) in the far-ultraviolet (FUV) and near-ultraviolet (NUV) bands (Bianchi et al. 2017), from Pan-STARRS in the *grizy* filters (Flewelling 2018), and from CatWISE in the W1 and W2 bands (Wright et al. 2010; Eisenhardt et al. 2020), covering the UV to infrared. These data are summarized in Table 1. We add a base error of 0.03 mag in quadrature to the existing errors to take into account systematics.

3. Analysis

In this section we describe the steps followed in deriving the stellar parameters of the primary using spectroscopic and photometric data. Following this, we combine the spectroscopic analysis with the analysis of the ellipsoidal variation from the photometric data to obtain the mass of the secondary.

[9] http://adina.feinste.in/eleanor/
[10] http://vizier.u-strasbg.fr/cgi-bin/VizieR

Table 1
Spectral Energy Distribution of SDSS J0229+7130

Filter	AB Magnitude
GALEX FUV	21.36 ± 0.25
GALEX NUV	20.80 ± 0.18
SDSS *u*	18.15 ± 0.03
SDSS *g*	16.62 ± 0.03
SDSS *r*	16.29 ± 0.03
SDSS *i*	16.17 ± 0.03
SDSS *z*	16.06 ± 0.03
Pan-STARRS *g*	16.62 ± 0.03
Pan-STARRS *r*	16.32 ± 0.03
Pan-STARRS *i*	16.17 ± 0.03
Pan-STARRS *z*	16.12 ± 0.03
Pan-STARRS *y*	15.98 ± 0.03
2MASS *J*[a]	16.23 ± 0.05
2MASS *H*[a]	16.50 ± 0.11
2MASS *Ks*[a]	17.07 ± 0.16
CatWISE W1[a]	17.56 ± 0.03
CatWISE W2[a]	18.34 ± 0.03

Note.
[a] Conversion from Vega to AB magnitude system is performed by using results from Jarrett et al. (2011) for the Wide-field Infrared Survey Explorer (WISE) and Blanton & Roweis (2007) for 2MASS.

3.1. Stellar Parameters

The SDSS spectra for the target show periodic shifts in the positions of absorption lines suggesting a varying RV. We choose to measure RV using Hα and Hβ simultaneously from SDSS-V spectra. We use just Hα in the APO spectra because the spectrum at the low-wavelength end is unreliable. We use `corv`[11] to measure the RVs for our SDSS and APO subexposures. `corv` computes the cross-correlation between the observed stellar spectrum and the template. For the template, we model each absorption line using two Voigt profiles with a common centroid. Once we obtain the RVs, we correct each spectrum for the Doppler shift associated with the measured RV and then coadd them in the target's rest frame. One of the SDSS subexposures has flux calibration issues and we do not include it in coadding, but we still use it for the RV measurements since the relative flux calibration does not affect the positions of the absorption lines. The coadded SDSS spectrum is shown in Figure 1.

Interestingly, the Na I D doublet near 5900 Å shows little sign of periodic variation, suggesting an interstellar origin rather than an association with the stellar photosphere. The measured temperature (>8000 K, Table 2) is also far too high to observe photospheric sodium lines (Yamaguchi et al. 2023). To verify this, we coadd $RV > 0$ subexposures and $RV < 0$ subexposures separately and compare the two. We confirm that the sodium absorption is stationary and is therefore associated with the interstellar medium. We then coadd all the spectra without shifting them to the rest frame of the primary and fit a Gaussian profile to the the Na I D lines. We obtain equivalent widths for D1, centered at 5897.5 Å, and D2, centered at 5891.6 Å, of 0.79 Å and 0.82 Å respectively, and 1.62 Å for the combined D1 + D2. Using the best-fit empirical relation between the Na I D equivalent widths and extinction from Poznanski et al. (2012), we derive the 2σ lower limit on the color excess, $E(B-V)$, to be 0.57, 0.31, and

[11] https://github.com/vedantchandra/corv

Table 2
Observed and Derived Parameters of SDSS J0229+7130

Parameter	Value
Gaia DR3 Source ID[a]	545437241454018304
R.A. (J2000)[a]	02:29:32.29
Decl. (J2000)[a]	+71:30:02.48
G (mag)[a]	16.28
$G_{BP} - G_{RP}$ (mag)[a]	0.77
d (pc)	1625^{+92}_{-92}
Orbital Parameters	
Period (hr)	35.8703 ± 0.0006
K (km s^{-1})	169 ± 3
Stellar Parameters	
$\log g_1$	4.11 ± 0.01
M_1 ($M_\odot$)	0.18 ± 0.02
M_2 ($M_\odot$)	$1.19^{+0.21}_{-0.14}$
R_1 ($R_\odot$)	0.62 ± 0.04
$T_{\rm eff}$ (K)	8567 ± 20[b]
$E(B-V)$	0.41 ± 0.01
[Fe/H]	-0.51 ± 0.03[b]
i (deg)	70^{+11}_{-8}

Notes.
[a] Gaia Collaboration et al. (2023).
[b] The reported errors are numerical and could be underestimated. A more conservative error estimate would be 100 K and 0.1 dex—approximately half the BOSZ model grid spacing.

0.68 using D1, D2, and D1 + D2, respectively. The trace photospheric sodium may contribute to the absorption, and we have not incorporated the inherent error in the empirical relation, so these values are only used as indicators of high extinction, which needs to be carefully taken into account in the subsequent modeling of the system.

The Ca II K line at 3933.6 Å is from the stellar surface. This is a feature observed in many ELM WDs as seen in Gianninas et al. (2014). We find that this absorption feature shows clear RV variation.

Using 1D hydrogen-atmosphere WD model spectra[12] (Koester 2010) to fit the spectrum gives a best-fitting model at the low-gravity edge of the model grid, $\log g = 5$. Therefore, to measure the stellar parameters, instead of using WD models we fit the spectrum with theoretical stellar models derived for main-sequence stars with lower surface gravity, as one would expect for pre-ELM objects, and with varying metallicity. To generate theoretical spectra we use the BOSZ grid (Bohlin et al. 2017). We use a grid with temperatures between 6000 K and 12,000 K, $\log g$ between 2 and 5, and [Fe/H] between −2.25 and 0.5, with a spacing of 250 K, 0.5 dex, and 0.25 dex, respectively.

We start with theoretical spectra with resolution $R \sim 10{,}000$, which are downgraded versions of theoretical spectra with $R \sim 30{,}000$ provided by Bohlin et al. (2017), i.e., much greater than the SDSS spectra. We convolve the theoretical spectra with a Gaussian to match the SDSS resolution $R \sim 2000$. Finally, we use the `scipy` function `RegularGridInterpolator`[13] (Weiser & Zarantonello 1988; Virtanen et al. 2020) to interpolate between the stellar parameter grid points. We then fit the coadded SDSS spectrum with the interpolated and convolved theoretical spectra to obtain the best-fit $\log g$, temperature, and metallicity of the star.

For the actual fitting, we minimize the χ^2 between the rest-frame coadded SDSS spectrum and the theoretical spectra. The SDSS spectrum can have flux calibration issues and the extinction is not well determined. To take into account these long-wavelength features we multiply the theoretical spectrum by a polynomial that is a function of wavelength. We examine the solution to make sure that the polynomial only corrects the long-wavelength features and does not overfit the absorption lines. The results are presented for polynomial of order 6, the lowest order which gives a stable solution. The spectroscopic log-likelihood to maximize is given by

$$\log \mathcal{L}_{\rm spec}(T_{\rm eff}, \log g, [{\rm Fe/H}]) = -\frac{1}{2}\sum_i \frac{(f_{\rm theo}(\lambda_i) - f_{{\rm obs},i})^2}{\sigma^2_{{\rm obs},i}} - \frac{1}{2}\ln(2\pi\sigma^2_{{\rm obs},i}), \quad (1)$$

where $f_{\rm theo}(\lambda_i)$ is the theoretical spectrum evaluated at different wavelengths, while $f_{{\rm obs},i}$ and $\sigma_{{\rm obs},i}$ are the spectral flux densities and the associated errors at those wavelengths, respectively.

We fit the extinction-corrected photometric magnitudes to obtain the radius, temperature, and $\log g$ of the primary. We estimate the extinction using the Green et al. (2019) model, which is a 3D dust map derived from Pan-STARRS. The extinction calculation is done using the `dustmaps`[14] (Green 2018) and `pyextinction`[15] packages. We infer the $(B-V)$ color excess using $E(B-V) = 0.884 \times \alpha$, where α is the dust reddening returned by the `dustmaps` package and represents the dust density along the line of sight (Green et al. 2018). We then use a Fitzpatrick (1999) extinction curve with $R_V = 3.1$ to obtain the extinction in various filters. The Green et al. (2019) dust map is probabilistic and there is a spread associated with the predicted extinction. We use the median of all returned samples of α by `dustmaps` to calculate the color excess. Additionally, the conversion from the α values from Green et al. (2019) to $E(B-V)$ or the value of R_V has uncertainty due to the varying dust size distribution and the resulting varying extinction curves. To take all of this into account we assign a conservative error of 20% to the median value provided by `dustmaps`. We use a Gaussian prior for $E(B-V)$ with mean and σ calculated as described above and leave it as nuisance parameter in our fitting. There are other 3D extinction maps such as those of Capitanio et al. (2017) and Lallement et al. (2019) which give somewhat different values for extinction. In particular, Lallement et al. (2019) predict a much larger extinction and disagreements between different extinction maps have been reported by them. We use the predictions from Green et al. (2019) for our fiducial solution and discuss the consequences of higher extinction in Section 4.

The theoretical spectra used for the photometric fitting are generated using the BaSeL library (Lejeune et al. 1997, 1998), which are photometrically corrected semiempirical models. The theoretical models estimate the flux from the stellar surface. We can multiply this by a factor of $(R/d)^2$ to obtain the apparent

[12] http://svo2.cab.inta-csic.es/theory/newov2/index.php?models=koester2
[13] https://docs.scipy.org/doc/scipy/reference/generated/scipy.interpolate.RegularGridInterpolator.html
[14] https://dustmaps.readthedocs.io/en/latest/
[15] https://github.com/mfouesneau/pyextinction

flux, where R is the radius of the primary and d is the distance to the object. The computation is performed using the package `pystelllibs`.[16] We use the Gaia parallax and include the distance as a nuisance parameter using the prior provided by Bailer-Jones et al. (2021). We then use the `pyphot`[17] package to integrate the theoretical spectra through the appropriate filters, and fit the extinction-corrected magnitudes with the theoretical magnitudes to estimate the best-fit parameters. The actual fitting is again performed by likelihood maximization. We find that the photometric fits very weakly depend on metallicity, Z, and thus we can fix $Z = 0.014$ without affecting our results significantly. The likelihood, $\mathcal{L}_{\rm phot}$, is defined similarly to the spectroscopic likelihood, replacing fluxes with appropriate magnitudes.

Finally, we perform joint spectrophotometric fitting by defining the combined likelihood as $\mathcal{L}(T_{\rm eff}, \log g, [{\rm Fe/H}], R, d, E(B-V)) = \mathcal{L}_{\rm phot} \times \mathcal{L}_{\rm spec} \times \mathcal{L}_{\rm priors}$. $\mathcal{L}_{\rm priors}$ is the likelihood associated with the priors for extinction and parallax as described earlier, and also the uniform priors for the rest of the parameters with limits set by the BOSZ grid. For the fitting, we calculate log likelihoods for each of these separately and add them. The posterior distribution is explored using `emcee`[18] (Foreman-Mackey et al. 2013).

The results from fitting the spectroscopic and photometric data alone showed the existence of two local minima centered around color excesses of 0.41 and 0.51, and a degeneracy between $E(B-V)$ and other stellar parameters. In Section 3.3, we combine the spectrophotometric data with the lightcurve and RV data and fit them simultaneously. To this end, we explore solutions around both these minima separately by restricting the color excess to the values above and setting a nominal error of 5%.

3.2. Lightcurve and Orbital Parameters

We can derive the orbital parameters by analyzing the RV and lightcurve data. The sampling of the RVs from spectroscopy is insufficient for deriving the period, and therefore we use the lightcurve data to measure the period. Stars in close binary systems show periodic changes in flux due to eclipses, heating of the companion due to the primary (reflection binary; Vaz 1985; Schaffenroth et al. 2022), or distortions of their surfaces induced by the tidal forces of the companion (ellipsoidal modulation; Kopal 1959; Green et al. 2023). We combine the data from both the g and r filters of ZTF and normalize the data to capture only the fractional variations about the median flux. We then use a Lomb–Scargle periodogram to derive the period of the orbit, and phase fold both the lightcurve as well as the RV data to this period. The periodogram is shown in Figure 3. The amplitude of the flux variation can differ depending on the filters used. However, for the purpose of period determination, we choose to collate data from both filters and treat them as single data set. This results in a more robust period determination while having negligible downsides.

Depending on the physical reasons that cause the flux variability, the orbital period of the system can correspond to the peak of the periodogram or be twice as long. The dominant effect of the tidal distortion is to produce a prolate ellipsoid pointed at the companion and this produces a quasi-sinusoidal variation in the emitted flux due to a varying surface area. As discussed in El-Badry et al. (2021), the quasi-sinusoidal variation would have different minima at two different end-on configurations (when the longest axis of the ellipsoid is directed toward the observer) due to different gravity darkening. However, this is a second-order effect which could be virtually invisible in a noisy lightcurve. If the minima are not distinguishable, then the periodogram peaks at half the orbital period. We find that phase folding to the period $P = 35.8703$ hr, twice the period corresponding to the maximum power of the periodogram, fits both the lightcurve and the RV data well, and the resulting fit is shown in Figure 4.

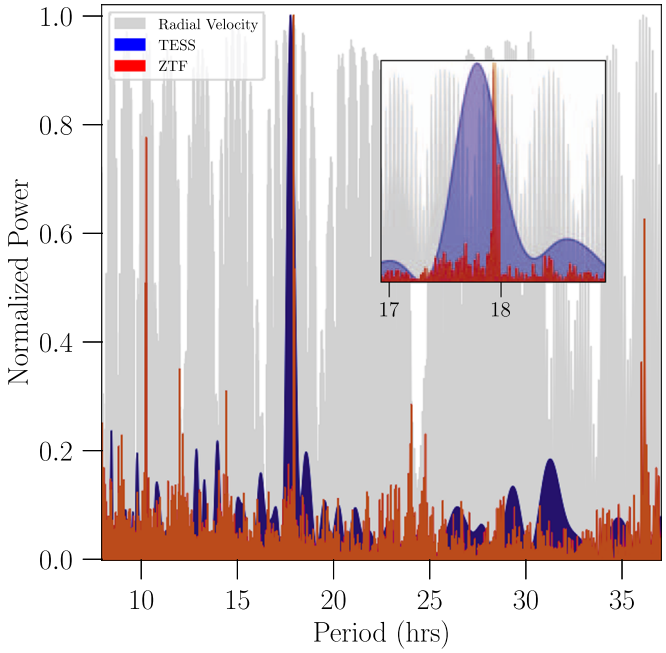

Figure 3. The normalized periodograms from various data sets: blue for TESS photometry, red for ZTF photometry, and gray for spectroscopy.

The variation of both data sets behave as we would theoretically expect for ellipsoidal variation—with one of the maxima of the lightcurve aligning with the minimum of RV curve and the other maximum coinciding with the RV maximum. This strongly supports our argument that the origin of the photometric variation is orbital in nature and is due to ellipsoidal variation. We do not observe any signs of eclipses, which would be signaled by a difference in the depth of the minima. When we fold the data to the period corresponding to the maximum power in the periodogram, we find that the RV data are not well fit. This rules out the possibility of a reflection binary, where the photometric variability is due to differences in the temperature of the primary and the companion (Wilson 1990). For systems where only one of the binary stars is visible, the reflection effect is seen for very hot primaries (>30,000 K; Hilditch et al. 1996). Since this is not the temperature regime we are dealing with, it is reasonable that photometric variability due to reflection is not the dominant effect in our source.

To verify the obtained period, we repeat the process with TESS data. There are two objects at 12″ and 19″ from our target, while each TESS pixel covers a region of 21″. Hence, the observed flux from our source is blended with that of the contaminants and the absolute flux variability measured by

[16] https://mfouesneau.github.io/pystellibs/
[17] https://mfouesneau.github.io/pyphot/
[18] https://emcee.readthedocs.io/en/stable/

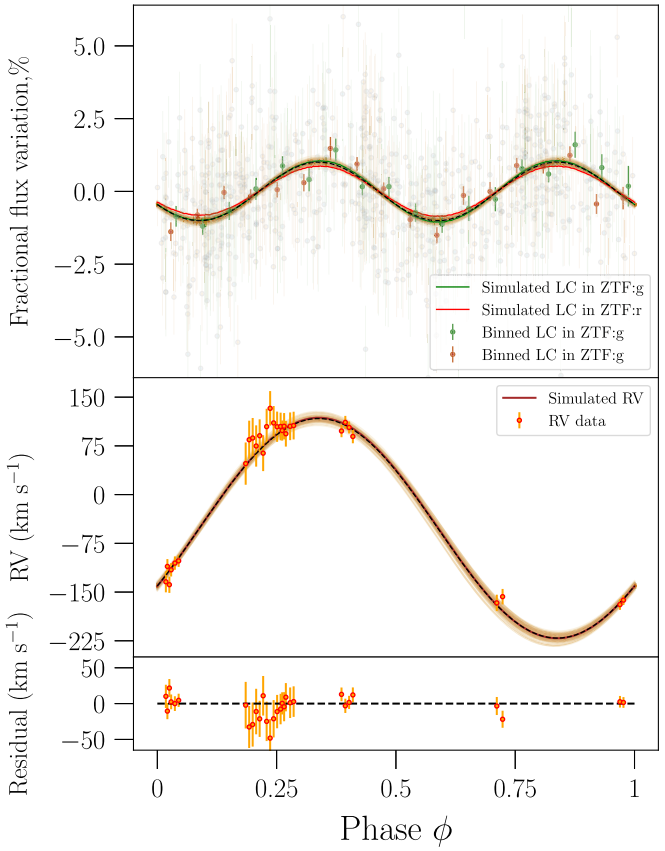

Figure 4. RV and ZTF lightcurve phase folded at the best period. In the top plot, solid data points are the binned lightcurve while the raw data are plotted in the background. We plot the PHOEBE simulated RV and lightcurve data for the best-fit parameters. In the top two panels, for comparison, we also plot the best-fit sinusoidal models as black dashed lines and also plot 100 random samples of sinusoidal models, in orange, as representative of the errors involved.

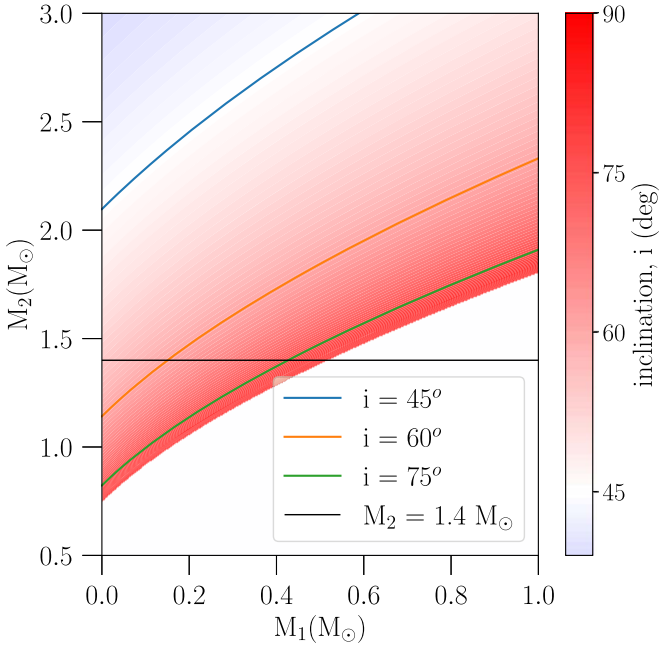

Figure 5. The parameter space of masses of the binaries allowed by the binary mass function. M_1 is the mass of the visible star, M_2 is the mass of the invisible companion, and i is the orbital inclination counted from the plane of the sky. The colored regions are allowed while the white region in the bottom right would require an unphysical $\sin i > 1$. We also show the Chandrasekhar limit (1.4 $M_\odot$) for M_2.

TESS does not accurately represent the variability of our target. Therefore, we analyze the TESS lightcurve separately from the ZTF lightcurve to account for the potential blending with nearby sources. Indeed, we find that the fractional variability of the TESS lightcurve is about 0.4%, much smaller than that of the ZTF lightcurve (2%). Thus, we restrict ourselves to using the ZTF data for further analysis while using TESS data to verify the period. We obtain periods of 35.8703 ± 0.0006 hr and 35.56 ± 0.07 hr from the ZTF and TESS data, respectively.

From the Lomb–Scargle periodogram, we compute the unnormalized power spectral density—which is proportional to χ^2 defined between the lightcurve data and the periodogram model (Scargle 1982; VanderPlas 2018). To estimate the errors, we calculate the frequencies where this χ^2 increases by a magnitude of 1 from the minimum. While there is a mismatch in the derived periods, at the 5σ level they are not inconsistent. Using TESS data we also verify that the period of 36 hr is robust and not associated with aliasing because of the different cadences associated with each data set.

Once we obtain the period, to measure the amplitude of variation and to verify that the periodicity is indeed due to ellipsoidal variation, we refit the lightcurve and RV data with a sinusoid (i.e., assuming eccentricity $e = 0$)—first individually and then both simultaneously. We fix the period and use the phase-folded data while leaving the semiamplitude of the flux variation, RV semiamplitude (K), systemic velocity (v_γ), and phase (ϕ) as free parameters. We find that both variations behave exactly as we expect and are exactly in phase. We also find that the flux of our target varies by about $(2.02 \pm 0.14)\%$ from the minimum to the maximum of the lightcurve and the RV semiamplitude is $K = (169 \pm 4)$ km s^{-1}. Once we know the RV semiamplitude, orbital period, and mass of one of the stars we can use the binary mass function to express the inclination in terms of the mass of the second star as

$$i = \arcsin\left(\left(\frac{(M_1 + M_2)^2}{M_2^3}\frac{P_{\rm orb}K^3}{2\pi G}\right)^{1/3}\right). \quad (2)$$

Figure 5 illustrates the parameter space that we need to explore. We see that based on the relatively long period combined with a relatively large RV variation, the secondary must be quite massive. Normally, one of the constraints on masses would be that the star should not overflow its Roche lobe radius (Eggleton 1983). However, in our case, the period of the binary is quite large and hence the orbital separation for reasonable masses (primary mass $M_1 > 0.1$ $M_\odot$ and secondary mass $M_2 > 1$ $M_\odot$) is large enough that the Roche lobe radius is much larger than the radius of the star and this constraint is never important.

Figure 5 gives a lower limit on the secondary mass M_2 of about 0.8 $M_\odot$. Given that we only see the primary, we suspect that the companion is a compact object. For any star, flux near the Rayleigh–Jeans tail of the stellar spectrum is proportional to R^2T. Thus, the ratio between the flux of two stars at large wavelengths can be written as $(R_1/R_2)^2(T_1/T_2)$. We can use this to our advantage and rule out main-sequence companions. If the companion is a 0.8 $M_\odot$ main-sequence star—which is the lowest possible companion mass allowed by the RV measurements—the radius and temperature are approximately equal to 0.7 $R_\odot$ and 0.84 $T_\odot$, respectively. Using the derived mass and

temperature of the primary, we get the flux ratio of the main-sequence companion to the primary to be 0.83. So the main-sequence companion contributes almost as much as the primary at long wavelengths and the total flux of the system would be twice the expected flux from the primary. We do not see such behavior in the 2MASS or WISE photometry. For higher companion masses, this effect would be more pronounced. Thus, we rule out a main-sequence companion for this system.

Depending on the composition, the maximum mass of a WD ranges between 1.35 and 1.40 $M_{\odot}$ (Caiazzo et al. 2021). Figure 5 indicates that for nearly edge-on orbits there is a possibility of the companion being a massive WD. For all moderate inclinations we expect the companion to be more massive than any reasonable limit on the WD mass, and therefore it would need to be an NS.

Along with the RVs we also use the lightcurve data to constrain the mass of the companion by simulating the lightcurves and RV variation. To simulate the periodic ellipsoidal variation we use `PHOEBE`[19] (Prša 2018). The stellar and orbital parameters are also taken as inputs to `PHOEBE` to simulate the lightcurve and the RV variation. To make this process computationally efficient, after phase folding the lightcurve we bin it into 2 hr time bins using `lightkurve` (Lightkurve Collaboration et al. 2018), reducing the total number of data points from 821 to 36.

If the secondary is a compact object, then for $M_2 \sim 0.9\ M_{\odot}$, an upper limit on the radius of the secondary of about $0.008\ R_{\odot}$ can be obtained from the mass–radius relation of WDs (Chandra et al. 2020), and the flux change due to the eclipse of primary due to secondary would be about 0.02% for edge-on orbits, which is much smaller than the sensitivity of our data. Therefore, we would not see eclipses even if the system was edge on, and therefore the lack of eclipses does not provide a constraint on the inclination. The same is true for microlensing as its effect is of the same order as eclipses (Marsh 2001). Limb darkening and gravity darkening are second-order effects and given the small amplitude of variation and noisiness of our data their effects are nearly negligible as well. Thus we model the surface using the default CK2004 atmospheric models (Castelli & Kurucz 2003) provided in `PHOEBE`, which includes gravity and limb darkening, even though these effects are small. The two solutions obtained in Section 3.1 from fitting the spectroscopic and the photometric data indicated that our target has temperature $T > 8000$ K. Thus we use a purely radiative atmospheric model with gravity darkening coefficient $\beta = 1$ (von Zeipel 1924; Claret 1999). We simulate the lightcurve in the ZTF g and r bands and fit them to the observed lightcurve.

Since the effects of limb darkening and gravity darkening are small, the dependence of the lightcurve on temperature is also minimal; the `PHOEBE`-generated lightcurves showed this behavior. Therefore, we fix the temperature of the primary to 8500 K and 10,000 K, for two solutions respectively, based on the spectrophotometric value obtained in Section 3.1 for ease of computation with little downside. We leave the surface gravity, radius of the primary, mass of the secondary, and the inclination as free parameters. In addition to these, we also leave the systemic velocity, v_{γ}, and initial phase of the orbit, $t_{0,\mathrm{sup-conj}}$, as free parameters.

[19] http://phoebe-project.org/

3.3. Combined Fit

With all the data sets assembled, we finally perform joint fitting where we add all the log likelihoods and the associated log priors, and maximize the resulting likelihood using `emcee`. Each data set constrains different stellar and orbital parameters in a distinct way. The spectroscopic fit constrains T_{eff}, $\log g$, and [Fe/H] independent of extinction. The lightcurve and RV fits also constrain $\log g$ and the radius of the primary independent of extinction, and also constrain M_2 and the inclination. The photometric fit is most sensitive to extinction and constrains T_{eff}, $\log g$, [Fe/H], R, and $E(B-V)$.

We explore two solutions, centered around the two local minima we found from the initial spectrophotometric fitting in Section 3.1 separately. The solution with the lower extinction value results in a primary mass of 0.18 $M_{\odot}$ and temperature ~ 8500 K, while the solution with higher extinction value results in a primary mass of 0.35 $M_{\odot}$ and temperature $\sim 10{,}000$ K. Looking at the final fits to the lightcurve and based on the theoretical expectations and empirical data on such binary systems we present the solution with the lower extinction value as the fiducial solution. We explain this choice in Section 4.4.

The results are tabulated in Table 2 and the combined fit is shown in Figures 1 and 4. The posterior distributions of the stellar parameters are shown in Figure 6. The mass of the primary is found to be $M_1 = 0.18\ M_{\odot}$ and the mass of the secondary to be $M_2 = 1.19\ M_{\odot}$, with a 1σ upper limit of 1.41 $M_{\odot}$ and a 3σ lower limit around 0.9 $M_{\odot}$ as shown in Figure 7, suggesting a massive WD or an NS companion. The 1σ errors reported are calculated at 16th and 84th percentile of the posterior distributions.

4. Discussion

In this paper we present the detection of a pre-ELM WD in a binary with a massive compact companion—likely a massive WD or an NS. We perform a joint analysis of the RV curve and of the photometric lightcurve of the visible pre-ELM WD to determine the allowed range of the masses of companion and find it to be $1.19^{+0.21}_{-0.14}\ M_{\odot}$.

4.1. Formation Scenarios

The formation of such systems has been theoretically studied in detail as ELM WDs were found in binaries with pulsars and WDs (Liu & Chen 2011; Shao & Li 2012; Istrate et al. 2014a; Li et al. 2019). We follow the various evolutionary tracks derived in these works and piece together the evolutionary pathway of our target. Both ELM WD–WD double degenerate binaries and ELM WD–NS binaries can form via two channels —stable Roche lobe overflow or common envelope ejection— both of which involve the massive compact companion accreting mass from a main-sequence star (Nelson et al. 2004; Istrate et al. 2014a; Li et al. 2019). Following the results from Li et al. (2019), we see that the large-period (>8 hr) and ELM WDs with WD companions could have formed only via the Roche lobe channel. While the formation channel involving common envelope ejection is not well studied, especially with NS companions (Istrate et al. 2016), the common envelope ejection channel is unlikely to produce the orbital period and primary mass combination that we observe. Thus, regardless of whether the unseen companion in our target is a massive WD or an NS, we suggest that the system formed via a stable Roche

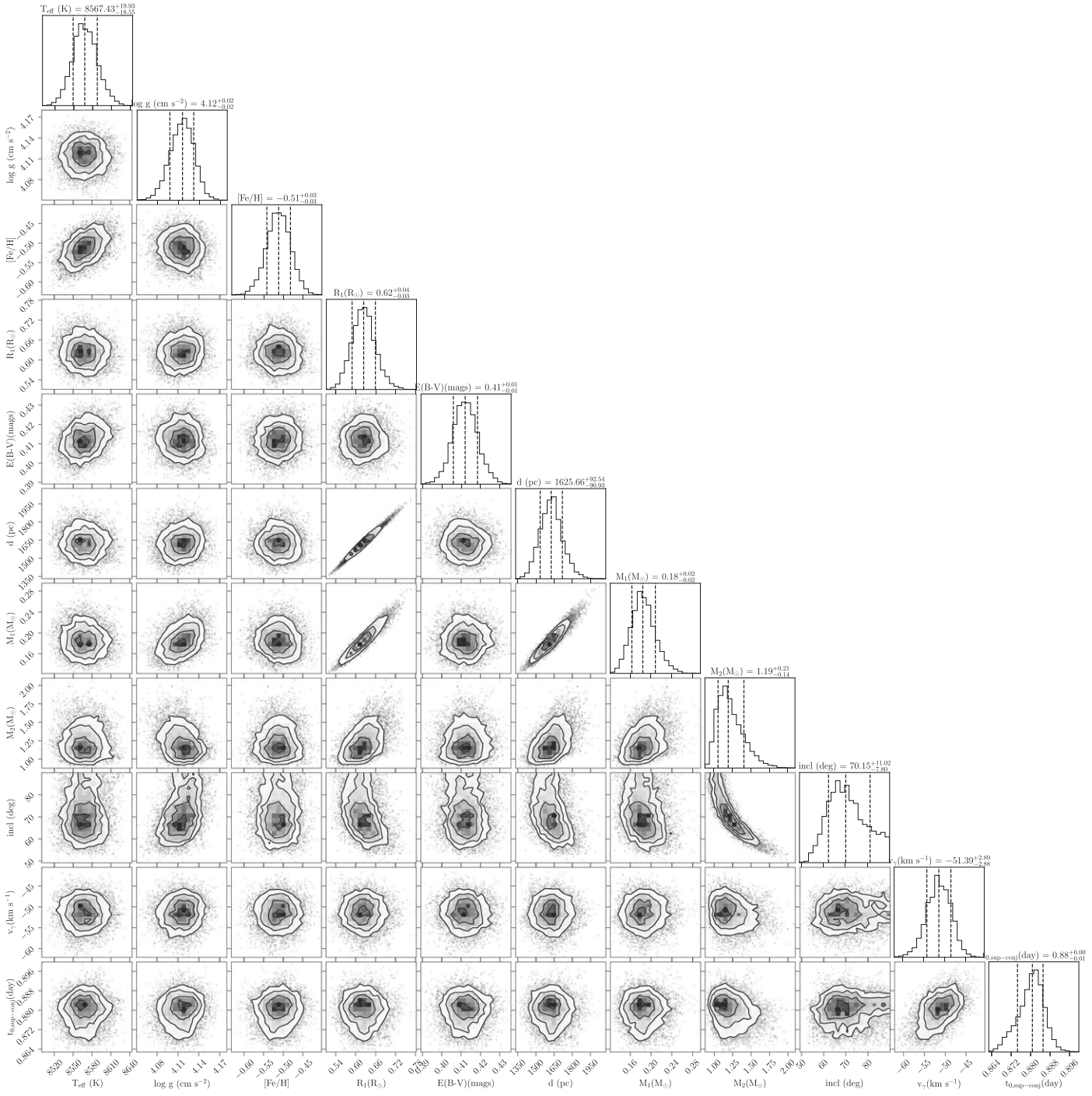

Figure 6. Posterior distribution from the joint parameter fitting of the spectroscopic, photometric, RV, and lightcurve data sets.

lobe overflow from the main-sequence star (which later became the primary pre-ELM WD) to the compact companion. Based on the final orbital periods, masses, and evolutionary models of Li et al. (2019), we deduce that the system must have arisen from a binary with an initial orbital period of the same order as the final orbital period, with the initial mass of the primary between 1.2 and 2 $M_{\odot}$.

4.2. Nature of the Companion

So far we have guessed the initial properties of the binary regardless of the nature of the companion. The initial companion mass is sensitive to the nature of the companion. Following Li et al. (2019), we find that if the companion is a WD, then its initial mass pre-Roche lobe interaction is around 0.6–0.8 $M_{\odot}$. WDs less massive than this range cannot accrete enough mass to grow to the observed mass of >1 $M_{\odot}$ because the mass accumulation is limited by the hydrogen burning rate on the surface of the WD and by the resulting stellar winds. WDs which are more massive than this range cannot appreciably gain mass due to hydrogen-shell flashes causing inefficient mass accumulation. If the companion is an NS, the results from Shao & Li (2012) suggest that a 1.1–1.2 $M_{\odot}$ NS in a binary system with properties similar to those of our target can accrete about 0.3 $M_{\odot}$ worth of mass over the course of the

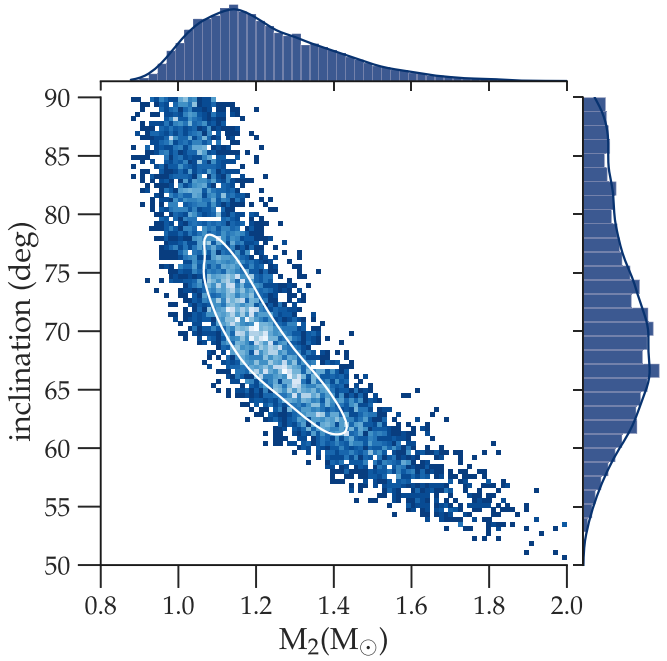

Figure 7. Distribution of M_2 against inclination. In white we show the 1σ contour.

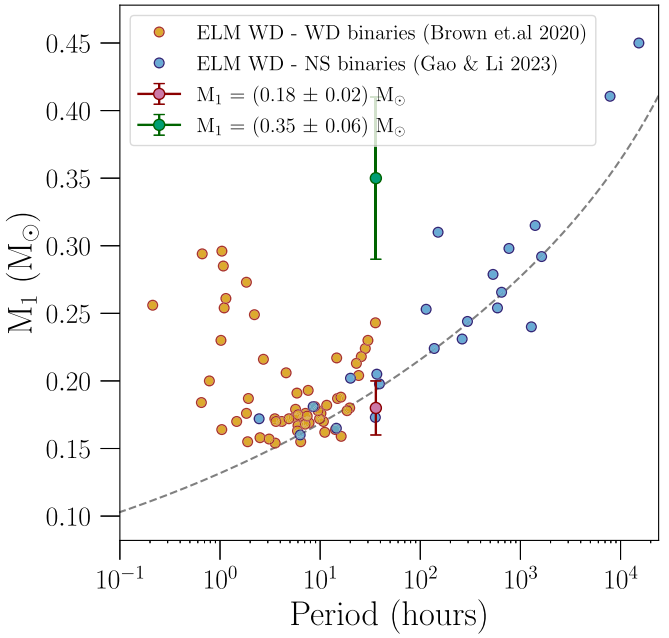

Figure 8. Masses vs. orbital periods for ELM WDs binaries are plotted along with both solutions obtained for our target. Binaries with WD companions are selected from Brown et al. (2020), while binaries with NS companions are selected from Gao & Li (2023). The dashed line is the theoretical mass–orbital period relation for the Roche lobe channel from Gao & Li (2023).

evolution of the ELM WD and lead to a system like ours. While the exact parameter values depend on various factors such as the magnetic braking index, metallicity, and, more importantly, on the exact nature of the companion, these are representative values characteristic of systems such as our target and which suggest plausible scenarios from which such systems could have evolved.

If the companion is an NS, the accretion of 0.3 $M_\odot$ worth of mass would spin up the NS and lead to a millisecond pulsar with a spin period of a few milliseconds (Liu & Chen 2011). The system is not detected in the NRAO VLA Sky Survey (Condon et al. 1998) at 1.4 GHz down to the ∼2.5 mJy flux level. X-ray signals can be expected from the surfaces of pulsars, especially from the magnetosphere of their polar caps in the case of recycled pulsars (Zavlin et al. 2002; Zavlin 2006; Kilic et al. 2011). Looking at data from an X-ray survey conducted with ROSAT (Truemper 1982) we find no X-ray signal near our target. However, these are all-sky surveys with short exposure times and consequently high flux limits and thus only the brightest pulsars would be visible (Danner et al. 1994; Becker et al. 1996). Using the ROSAT flux limit of 10^{-13} erg cm^{-2} s^{-1} and assuming zero extinction at X-ray wavelengths we obtain an upper limit on the X-ray luminosity of $L_X < 3.5 \times 10^{31}$ erg s^{-1}. Typical millisecond pulsars have X-ray luminosities below this limit (Bogdanov et al. 2006; Lee et al. 2018) and therefore would remain undetected. The presence of extinction would make their detection by ROSAT even more difficult.

As has been previously observed, the eccentricity of a system similar to ours is very small (Edwards & Bailes 2001; Istrate et al. 2014a). The binary must have gone through a common envelope phase before the more massive companion formed a compact remnant (Li et al. 2019), resulting in a circular orbit. While one would expect that the formation of an NS would give a kick to the primary leading to an eccentric orbit, the subsequent Roche lobe overflow would circularize the orbit, as has been observed for such binaries. The phase-folded RV curve and the lightcurve we obtain are consistent with a circular orbit. In principle, the eccentricity could be left as a free parameter in the analysis. However, given the strong theoretical footing for a nearly zero eccentricity, we do not expect the results to change in a significant way and leave it at zero.

4.3. Nature of the Primary

While we have assumed that the primary is a pre-ELM WD, we can verify our assumptions using derived parameters. Based on the large observed brightness (∼1.5 $L_\odot$) and low mass, the primary cannot be a main-sequence star. In addition, the primary is too cold and much less massive than an sdB star ($T_{sdB} > 20{,}000$ K and $M_{sdB} \sim 0.5$ $M_\odot$; Heber 2009). We conclude that despite its position on the color–magnitude diagram (Figure 2), which is close to the main-sequence track, the primary is indeed a pre-ELM WD. We also see that the primary has an anomalously large luminosity (or, equivalently, a larger radius) compared to the pre-ELM sample of El-Badry et al. (2021), including those which are still mass transferring. This can be explained in the context of the Roche lobe channel as well: our target has a much greater orbital period compared to their sample, and consequently during the binary evolution the Roche lobe mass transfer is expected to terminate earlier, leading to a larger radius.

4.4. Comparison with Theoretical Models

The final stage of the close binary evolution through Roche lobe overflow results in a relationship between the primary masses and the orbital periods. These values are shown in Figure 8, where we compare our target with ELM WD–WD binaries from an ELM survey (Brown et al. 2020) and ELM WD–NS binaries from Gao & Li (2023). The short-period binaries ($P < 8$ hr) with a broad distribution of primary masses

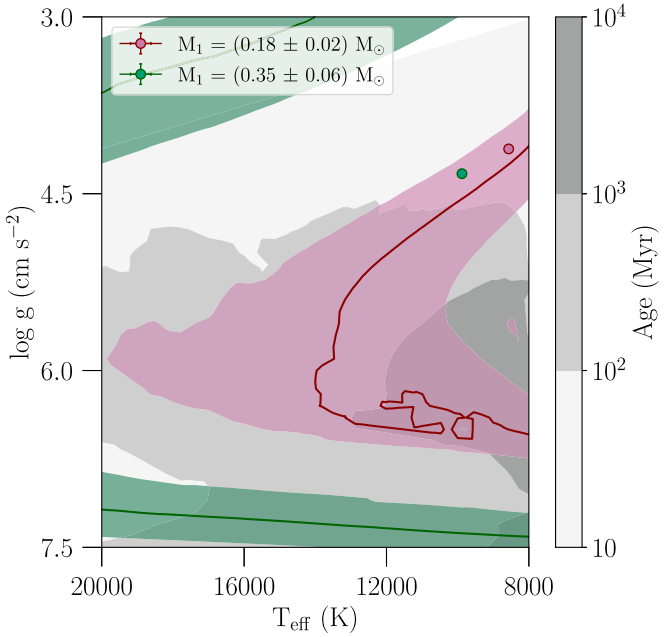

Figure 9. Cooling curves and ages for ELM WDs from models by Althaus et al. (2013) are shown in this figure. The pink solid line is the cooling curve for a 0.18 $M_\odot$ ELM WD and the pink band corresponds to cooling curves for masses in the range of 0.16–0.2 $M_\odot$ ELM WDs. The green solid line is the cooling curve for a 0.35 $M_\odot$ ELM WD and the green band corresponds to cooling curves for masses in the range of 0.29–0.41 $M_\odot$ ELM WDs. The results for both solutions are also plotted. The age ranges for ELM WDs are shown in various shades of gray contours.

are from the common envelope channel, whereas the Roche lobe channel forms a relatively narrow locus of objects with a strong mass–period dependence. Our target with its period of $P = 35.87$ hr falls in the long-period region of the expected Roche lobe channel track. For comparison, we show the theoretically expected mass–period relations from binary simulations consisting of an NS and a WD primary.

In Figure 9, we show cooling curves and ages for ELM WDs from Althaus et al. (2013). We see that the target is currently younger than 100 Myr and is in its contraction stage. Using the models of Istrate et al. (2014b), we suggest that the primary will cool down, contract, and settle onto the WD cooling track in a time of the order of 0.2–2 Gyr. The gravitational-wave merger timescale for our target is of order a few hundred billion years. Comparing the two timescales we conclude that this system will end up as a stable binary consisting of an ELM WD and a massive compact object whose orbital period will remain at its current value for much longer than the Hubble time.

In Figures 8 and 9, we plot both obtained solutions. In Figure 8, the higher-mass solution, shown in green, is above the expected track, while the low-mass solution, shown in red, is consistent with the theoretical expectation. In Figure 9, the difference is even more stark—the low-mass solution is well within the expected theoretical cooling curves while the high-mass solution is clearly inconsistent. Therefore, while both solutions are statistically viable, the solution with the higher primary mass is inconsistent with the astrophysical evolutionary tracks, and we determine the mass of the primary to be $M_1 = 0.18\ M_\odot$.

4.5. Sources of Uncertainty

One of the major sources of error in our analysis is the estimation of extinction. As we have discussed, we tried to take into account the various uncertainties associated with it. The uncertainty in the extinction along the line of sight and the degeneracy between the color excess and other stellar parameters gives two local χ^2 minima in the multidimensional parameter space of the fit. High values of extinction are not ruled out based on the value of χ^2 or of the likelihood. The high-extinction solution has a higher mass (Section 3.3), and looking at Figures 8 and 9, we find this solution (shown in green) is not favored by the models. Following Figure 5, a lower primary mass suggests a lower secondary mass and thus the low extinction solution weakens the case for an NS companion.

In addition to the extinction, the other uncertain part is the polynomial fitting of the continuum. While we have presented results for the polynomial of order 6, we refit the spectrum by increasing the order of the polynomial to make sure this is a stable solution. We find that the final primary mass does not change appreciably and remains within 1σ of our quoted value. We therefore present the results from fitting with the lowest-order polynomial which gives a stable solution. We also performed our analysis by fitting continuum-normalized absorption lines alone instead of the full spectral fitting. This technique was sensitive to the choice of absorption lines and to the the continuum normalization. We did manage to recover our solution—albeit with a higher uncertainty, making it less reliable than our fiducial solution.

Acknowledgments

G.A.P. thanks W. Brown for useful comments. V.C. gratefully acknowledges a Peirce Fellowship from Harvard University. N.L.Z. acknowledges support by the JHU President's Frontier Award and by the seed grant from the JHU Institute for Data Intensive Engineering and Science. B.G. received funding from the European Research Council (ERC) under the European Union's Horizon 2020 research and innovation program (grant agreement No. 101020057). Y.Z. gratefully acknowledge support from NASA grants NNH17ZDA001N, 80NSSC22K0494, 80NSSC21K0242, and 80NSSC19K0112. N.R.C. is supported by the National Science Foundation Graduate Research Fellowship Program under grant No. DGE2139757. Any opinions, findings, and conclusions or recommendations expressed in this material are those of the authors and do not necessarily reflect the views of the National Science Foundation.

Based on observations obtained with the Samuel Oschin 48 inch Telescope at the Palomar Observatory as part of the Zwicky Transient Facility project. ZTF is supported by the National Science Foundation under grant No. AST-1440341 and a collaboration including Caltech, IPAC, the Weizmann Institute for Science, the Oskar Klein Center at Stockholm University, the University of Maryland, the University of Washington, Deutsches Elektronen-Synchrotron and Humboldt University, Los Alamos National Laboratories, the TANGO Consortium of Taiwan, the University of Wisconsin at Milwaukee, and Lawrence Berkeley National Laboratories. Operations are conducted by COO, IPAC, and UW.

This publication makes use of data products from the Two Micron All Sky Survey, which is a joint project of the University of Massachusetts and the Infrared Processing and Analysis Center/California Institute of Technology, funded by the National Aeronautics and Space Administration and the National Science Foundation.

Funding for the Sloan Digital Sky Survey V has been provided by the Alfred P. Sloan Foundation, the Heising-

Simons Foundation, the National Science Foundation, and the Participating Institutions. SDSS acknowledges support and resources from the Center for High-Performance Computing at the University of Utah. SDSS telescopes are located at Apache Point Observatory, funded by the Astrophysical Research Consortium and operated by New Mexico State University, and at Las Campanas Observatory, operated by the Carnegie Institution for Science. The SDSS website is www.sdss.org.

SDSS is managed by the Astrophysical Research Consortium for the Participating Institutions of the SDSS Collaboration, including Caltech, The Carnegie Institution for Science, Chilean National Time Allocation Committee (CNTAC) ratified researchers, The Flatiron Institute, the Gotham Participation Group, Harvard University, Heidelberg University, The Johns Hopkins University, L'Ecole polytechnique fédérale de Lausanne (EPFL), Leibniz-Institut für Astrophysik Potsdam (AIP), Max-Planck-Institut für Astronomie (MPIA Heidelberg), Max-Planck-Institut für Extraterrestrische Physik (MPE), Nanjing University, National Astronomical Observatories of China (NAOC), New Mexico State University, The Ohio State University, Pennsylvania State University, Smithsonian Astrophysical Observatory, Space Telescope Science Institute (STScI), the Stellar Astrophysics Participation Group, Universidad Nacional Autónoma de México, University of Arizona, University of Colorado Boulder, University of Illinois at Urbana-Champaign, University of Toronto, University of Utah, University of Virginia, Yale University, and Yunnan University.

Software: astropy (Astropy Collaboration et al. 2013, 2018, 2022), numpy (Harris et al. 2020), scipy (Virtanen et al. 2020), matplotlib (Hunter 2007), lightkurve (Lightkurve Collaboration et al. 2018), eleanor (Feinstein et al. 2019), and PHOEBE (Prša 2018).

Data Availability

The photometric data from GALEX, SDSS, Pan-STARRS, 2MASS, and CatWISE used in this paper are publicly available from the corresponding archives. The ZTF and TESS light-curve data used are also publicly available (STScI 2019, 2020; IRSA 2022). The SDSS-V data are not public but the reduced and calibrated data are made available in the online version of this article (see Figure 1). The APO data used in this work are also made available in the online version of this article.

ORCID iDs

Gautham Adamane Pallathadka https://orcid.org/0000-0002-5864-1332
Vedant Chandra https://orcid.org/0000-0002-0572-8012
Nadia L. Zakamska https://orcid.org/0000-0001-6100-6869
Hsiang-Chih Hwang https://orcid.org/0000-0003-4250-4437
Yossef Zenati https://orcid.org/0000-0002-0632-8897
J. J. Hermes https://orcid.org/0000-0001-5941-2286
Kareem El-Badry https://orcid.org/0000-0002-6871-1752
Boris T. Gänsicke https://orcid.org/0000-0002-2761-3005
Sean Morrison https://orcid.org/0000-0002-6770-2627
Nicole R. Crumpler https://orcid.org/0000-0002-8866-4797
Stefan Arseneau https://orcid.org/0000-0002-6270-8624

References

Ahumada, R., Allende Prieto, C., Almeida, A., et al. 2020, ApJS, 249, 3
Althaus, L. G., Miller Bertolami, M. M., & Córsico, A. H. 2013, A&A, 557, A19
Antoniadis, J., Freire, P. C. C., Wex, N., et al. 2013, Sci, 340, 448
Astropy Collaboration, Price-Whelan, A. M., Lim, P. L., et al. 2022, ApJ, 935, 167
Astropy Collaboration, Price-Whelan, A. M., Sipőcz, B. M., et al. 2018, AJ, 156, 123
Astropy Collaboration, Robitaille, T. P., Tollerud, E. J., et al. 2013, A&A, 558, A33
Bailer-Jones, C. A. L., Rybizki, J., Fouesneau, M., Demleitner, M., & Andrae, R. 2021, AJ, 161, 147
Becker, W., Trumper, J., Lundgren, S. C., Cordes, J. M., & Zepka, A. F. 1996, MNRAS, 282, L33
Bianchi, L., Shiao, B., & Thilker, D. 2017, ApJS, 230, 24
Blanton, M. R., & Roweis, S. 2007, AJ, 133, 734
Bobrick, A., Davies, M. B., & Church, R. P. 2017, MNRAS, 467, 3556
Bobrick, A., Zenati, Y., Perets, H. B., Davies, M. B., & Church, R. 2022, MNRAS, 510, 3758
Bogdanov, S., Grindlay, J. E., Heinke, C. O., et al. 2006, ApJ, 646, 1104
Bohlin, R. C., Mészáros, S., Fleming, S. W., et al. 2017, AJ, 153, 234
Bowen, I. S., & Vaughan, A. H. J. 1973, ApOpt, 12, 1430
Brasseur, C. E., Phillip, C., Fleming, S. W., Mullally, S. E., & White, R. L. 2019, Astrocut: Tools for Creating Cutouts of TESS Images, Astrophysics Source Code Library, ascl:1905.007
Brown, W. R., Kilic, M., Allende Prieto, C., & Kenyon, S. J. 2010, ApJ, 723, 1072
Brown, W. R., Kilic, M., Kosakowski, A., et al. 2020, ApJ, 889, 49
Caiazzo, I., Burdge, K. B., Fuller, J., et al. 2021, Natur, 595, 39
Capitanio, L., Lallement, R., Vergely, J. L., Elyajouri, M., & Monreal-Ibero, A. 2017, A&A, 606, A65
Castelli, F., & Kurucz, R. L. 2003, in IAU Symp. 210, Modelling of Stellar Atmospheres, ed. N. Piskunov, W. W. Weiss, & D. F. Gray (San Francisco, CA: ASP), A20
Chandra, V., Hwang, H.-C., Zakamska, N. L., & Cheng, S. 2020, ApJ, 899, 146
Claret, A. 1999, in ASP Conf. Ser. 173, Stellar Structure: Theory and Test of Connective Energy Transport, ed. A. Gimenez, E. F. Guinan, & B. Montesinos (San Francisco, CA: ASP), 277
Condon, J. J., Cotton, W. D., Greisen, E. W., et al. 1998, AJ, 115, 1693
Corrales, L. 2015, dust: Calculate the Intensity of Dust Scattering Halos in the X-ray, v1.0, Zenodo, doi:10.5281/zenodo.15991
Danner, R., Kulkarni, S. R., & Thorsett, S. E. 1994, ApJL, 436, L153
Edwards, R. T., & Bailes, M. 2001, ApJL, 547, L37
Eggleton, P. P. 1983, ApJ, 268, 368
Eisenhardt, P. R. M., Marocco, F., Fowler, J. W., et al. 2020, ApJS, 247, 69
El-Badry, K., Rix, H.-W., Quataert, E., Kupfer, T., & Shen, K. J. 2021, MNRAS, 508, 4106
Feinstein, A. D., Montet, B. T., Foreman-Mackey, D., et al. 2019, PASP, 131, 094502
Fitzpatrick, E. L. 1999, PASP, 111, 63
Flewelling, H. 2018, AAS Meeting, 231, 436.01
Foreman-Mackey, D., Hogg, D. W., Lang, D., & Goodman, J. 2013, PASP, 125, 306
Fryer, C. L., Woosley, S. E., Herant, M., & Davies, M. B. 1999, ApJ, 520, 650
Gaia Collaboration, Vallenari, A., Brown, A. G. A., et al. 2023, A&A, 674, A1
Gao, S.-J., & Li, X.-D. 2023, MNRAS, 525, 2605
Gianninas, A., Dufour, P., Kilic, M., et al. 2014, ApJ, 794, 35
Green, G. 2018, JOSS, 3, 695
Green, G. M., Schlafly, E., Zucker, C., Speagle, J. S., & Finkbeiner, D. 2019, ApJ, 887, 93
Green, G. M., Schlafly, E. F., Finkbeiner, D., et al. 2018, MNRAS, 478, 651
Green, M. J., Maoz, D., Mazeh, T., et al. 2023, MNRAS, 522, 29
Gunn, J. E., Siegmund, W. A., Mannery, E. J., et al. 2006, AJ, 131, 2332
Harris, C. R., Millman, K. J., van der Walt, S. J., et al. 2020, Natur, 585, 357
Heber, U. 2009, ARA&A, 47, 211
Hilditch, R. W., Harries, T. J., & Hill, G. 1996, MNRAS, 279, 1380
Hunter, J. D. 2007, CSE, 9, 90
Iben, I., & Tutukov, A. V. 1985, ApJS, 58, 661
IRSA 2022, Zwicky Transient Facility Image Service, IPAC, doi:10.26131/IRSA539
Istrate, A. G., Marchant, P., Tauris, T. M., et al. 2016, A&A, 595, A35
Istrate, A. G., Tauris, T. M., & Langer, N. 2014a, A&A, 571, A45
Istrate, A. G., Tauris, T. M., Langer, N., & Antoniadis, J. 2014b, A&A, 571, L3
Jarrett, T. H., Cohen, M., Masci, F., et al. 2011, ApJ, 735, 112
Jha, S. W., Maguire, K., & Sullivan, M. 2019, NatAs, 3, 706
Kaltenborn, M. A., Fryer, C. L., Wollaeger, R. T., et al. 2022, ApJ, 956, 71
Kanodia, S., & Wright, J. 2018, RNAAS, 2, 4

Kilic, M., Brown, W. R., Prieto, C. A., et al. 2011, ApJ, 727, 3
Koester, D. 2010, MmSAI, 81, 921
Kollmeier, J., Anderson, S. F., Blanc, G. A., et al. 2019, BAAS, 51, 274
Kollmeier, J. A., Zasowski, G., Rix, H.-W., et al. 2017, SDSS-V: Pioneering Panoptic Spectroscopy, arXiv:1711.03234
Kopal, Z. 1959, Close Binary Systems (London: Chapman & Hall)
Korol, V., Hallakoun, N., Toonen, S., & Karnesis, N. 2022, MNRAS, 511, 5936
Kupfer, T., Bauer, E. B., Burdge, K. B., et al. 2020a, ApJL, 898, L25
Kupfer, T., Bauer, E. B., Marsh, T. R., et al. 2020b, ApJ, 891, 45
Lagos, F., Schreiber, M. R., Parsons, S. G., Gänsicke, B. T., & Godoy, N. 2020, MNRAS, 499, L121
Lallement, R., Babusiaux, C., Vergely, J. L., et al. 2019, A&A, 625, A135
Lee, J., Hui, C. Y., Takata, J., et al. 2018, ApJ, 864, 23
Lejeune, T., Cuisinier, F., & Buser, R. 1997, A&AS, 125, 229
Lejeune, T., Cuisinier, F., & Buser, R. 1998, A&AS, 130, 65
Li, Z., Chen, X., Chen, H.-L., & Han, Z. 2019, ApJ, 871, 148
Lightkurve Collaboration, Cardoso, J. V. d. M., Hedges, C., et al. 2018, Lightkurve: Kepler and TESS Time Series Analysis in Python, Astrophysics Source Code Library, ascl:1812.013
Liu, W.-M., & Chen, W.-C. 2011, MNRAS, 416, 2285
Maoz, D., Mannucci, F., & Nelemans, G. 2014, ARA&A, 52, 107
Margalit, B., & Metzger, B. D. 2016, MNRAS, 461, 1154
Marsh, T. R. 2001, MNRAS, 324, 547
Marsh, T. R. 2011, CQGra, 28, 094019
Marsh, T. R., Dhillon, V. S., & Duck, S. R. 1995, MNRAS, 275, 828
Masci, F. J., Laher, R. R., Rusholme, B., et al. 2019, PASP, 131, 018003
Maxted, P. F. L., Anderson, D. R., Burleigh, M. R., et al. 2011, MNRAS, 418, 1156
Nelson, L. A., Dubeau, E., & MacCannell, K. A. 2004, ApJ, 616, 1124
Nomoto, K. 1984, ApJ, 277, 791
Ochsenbein, F., Bauer, P., & Marcout, J. 2000, A&AS, 143, 23
Poznanski, D., Prochaska, J. X., & Bloom, J. S. 2012, MNRAS, 426, 1465
Prša, A. 2018, Modeling and Analysis of Eclipsing Binary Stars (Bristol: IOP Publishing), 2514
Ricker, G. R., Winn, J. N., Vanderspek, R., et al. 2015, JATIS, 1, 014003
Scargle, J. D. 1982, ApJ, 263, 835
Schaffenroth, V., Pelisoli, I., Barlow, B. N., Geier, S., & Kupfer, T. 2022, A&A, 666, A182
Shao, Y., & Li, X.-D. 2012, ApJ, 756, 85
Skrutskie, M. F., Cutri, R. M., Stiening, R., et al. 2006, AJ, 131, 1163
Smee, S. A., Gunn, J. E., Uomoto, A., et al. 2013, AJ, 146, 32
Soker, N. 2019, NewAR, 87, 101535
STScI 2019, TESS Calibrated Full Frame Images: Sector 18, STScI/MAST, doi:10.17909/2H0M-QR07
STScI 2020, TESS Calibrated Full Frame Images: Sector 19, STScI/MAST, doi:10.17909/MSXY-D755
Truemper, J. 1982, AdSpR, 2, 241
VanderPlas, J. T. 2018, ApJS, 236, 16
Vaz, L. P. R. 1985, Ap&SS, 113, 349
Virtanen, P., Gommers, R., Oliphant, T. E., et al. 2020, NatMe, 17, 261
von Zeipel, H. 1924, MNRAS, 84, 665
Wang, L., Gies, D. R., Lester, K. V., et al. 2020, AJ, 159, 4
Weiser, A., & Zarantonello, S. E. 1988, MaCom, 50, 189
Wilson, J. C., Hearty, F. R., Skrutskie, M. F., et al. 2019, PASP, 131, 055001
Wilson, R. E. 1990, ApJ, 356, 613
Wright, E. L., Eisenhardt, P. R. M., Mainzer, A. K., et al. 2010, AJ, 140, 1868
Yamaguchi, N., El-Badry, K., Rodriguez, A. C., et al. 2023, MNRAS, 524, 740
Zavlin, V. E. 2006, ApJ, 638, 951
Zavlin, V. E., Pavlov, G. G., Sanwal, D., et al. 2002, ApJ, 569, 894
Zenati, Y., Bobrick, A., & Perets, H. B. 2020, MNRAS, 493, 3956
Zenati, Y., Perets, H. B., & Toonen, S. 2019, MNRAS, 486, 1805